Electronic Supplementary Information

Development of solar fuels photoanodes through combinatorial integration of Ni-La-Co-Ce oxide catalysts on $BiVO_4$

D. Guevarra, A. Shinde, S. K. Suram, I. D. Sharp, F. M. Toma, J. A. Haber, J. M. Gregoire

Material Characterization

This section provides supplementary information on quality control and visualization of the composition space. Table S1 lists 15 EDS composition measurements of metal oxides on $BiVO_4$ after inkjet printing and calcination. Table S2 lists the definition of composition symbols used to map the 4-component composition space as a series of 12 pseudo-ternary composition triangles. Figure S1 shows the results of XRD characterization and XRF mapping of the $BiVO_4$ film prior to deposition of the catalyst library. The XRD measurement was performed with a 0.5˚ incident angle to limit the sampling depth, and the resulting diffraction pattern demonstrates successful formation of the $BiVO_4$ phase with no detectable secondary phases. The combinatorial photoelectrochemical measurements rely on a uniform light absorber layer, and the uniformity of the $BiVO_4$ composition over the photoanode library region is demonstrated by the XRF measurement.

Table S1. EDS composition measurements of 15 metal oxides deposited onto $BiVO_4$. The maximum composition deviation of 0.06 and mean composition deviation of 0.034 are within the uncertainty of EDS composition measurements for thin, discontinuous films.

Library sample	EDS composition
$Ni_{0.5}Co_{0.5}O_x$-L1	$Ni_{0.56}Co_{0.44}$
$Ni_{0.5}Co_{0.5}O_x$ -L2	$Ni_{0.54}Co_{0.46}$
$Ni_{0.5}Co_{0.5}O_x$ -L3	$Ni_{0.49}Co_{0.51}$
$Ni_{0.5}La_{0.5}O_x$ -L1	$Ni_{0.56}La_{0.44}$
$Ni_{0.5}La_{0.5}O_x$ -L2	$Ni_{0.55}La_{0.45}$
$Ni_{0.5}La_{0.5}O_x$ -L3	$Ni_{0.55}La_{0.45}$
$Ni_{0.5}Ce_{0.5}O_x$ -L2	$Ni_{0.53}Ce_{0.47}$
$Ni_{0.5}Ce_{0.5}O_x$ -L3	$Ni_{0.49}Ce_{0.51}$
$La_{0.5}Ce_{0.5}O_x$ -L1	$La_{0.45}Ce_{0.55}$
$La_{0.5}Ce_{0.5}O_x$ -L3	$La_{0.48}Ce_{0.52}$
$La_{0.5}Co_{0.5}O_x$ -L1	$La_{0.53}Co_{0.47}$
$La_{0.5}Co_{0.5}O_x$ -L2	$La_{0.51}Co_{0.49}$
$La_{0.5}Co_{0.5}O_x$ -L3	$La_{0.55}Co_{0.45}$
$Co_{0.5}Ce_{0.5}O_x$ -L1	$Co_{0.52}Ce_{0.48}$
$Co_{0.5}Ce_{0.5}O_x$ -L3	$Co_{0.46}Ce_{0.54}$

Table S2: Definition of composition labels in Fig. 4a, where M' is the most M-rich composition with at least 0.1 of each element and M'' is the most M-rich composition with at least 0.2 of each element. The entire quaternary composition space with 0.1 composition intervals can be considered as the combined set of all pseudo-ternary combinations of (La-Ce-Ni-Co)O_x, of La'-Ce'-Ni'-Co', and of La''-Ce''-Ni''-Co''.

La′	$La_{0.7}Ce_{0.1}Ni_{0.1}Co_{0.1}O_x$
Ce′	$Ce_{0.7}La_{0.1}Ni_{0.1}Co_{0.1}O_x$
Ni'	$Ni_{0.7}Ce_{0.1}La_{0.1}Co_{0.1}O_x$
Co′	$Co_{0.7}Ce_{0.1}Ni_{0.1}La_{0.1}O_x$
La″	$La_{0.4}Ce_{0.2}Ni_{0.2}Co_{0.2}O_x$
Ce″	$Ce_{0.4}La_{0.2}Ni_{0.2}Co_{0.2}O_x$
Ni″	$Ni_{0.4}Ce_{0.2}La_{0.2}Co_{0.2}O_x$
Co″	$Co_{0.4}Ce_{0.2}Ni_{0.2}La_{0.2}O_x$

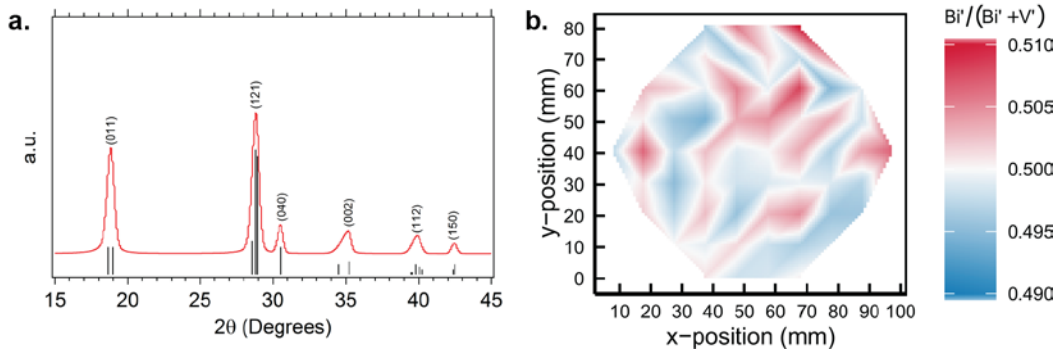

Figure S1. XRD characterization (a) and XRF mapping of the Bi:V composition (b) of the spin-coated $BiVO_4$ thin film prior to deposition of the metal oxide library. In the XRD measurement, the thin film XRD pattern (red) matches well with the desired monoclinic $BiVO_4$ phase (black lines, space group I2/b, JPCDS no. 04-010-5711). In the XRF measurement, the small deviations from the intended value of 0.5 are within the noise of the measurement, and the lack of a spatial gradient in composition demonstrates the uniformity of the spin coating process.

Optical data processing

In this section we describe the calibration of the illumination source used in the high throughput experiments, define the lamp spectra used in the calculations of optical properties, and show some representative spectra to illustrate the data processing.

An integrating sphere and spectrometer were calibrated using an illumination standard (Sun 3000 Solar Simulator, 19.0 A current, 1 sun). That is, the ratio of the measured spectrum to the known irradiance spectrum of this illumination source provided a calibration of spectral irradiance per count for the optical detection apparatus. This detection apparatus was then installed in the operational high throughput scanning droplet cell with fiber optic integrated illumination, shown in Fig. 1b. The illumination footprint on the substrate was measured to be a 1 mm-diameter circle. This 0.0079 cm^2 area was used to calculate both photocurrent density and spectral irradiance. The resulting spectral irradiance used in the high throughput experiment is shown in Figure S2 along with the AM 1.5 spectrum (ASTM 6173-03 standard for global air mass 1.5). In the useable wavelength range of this light source and detector (390-900 nm), the total irradiance from the high throughput experimental light

source is 1846 W m^{-2}, compared to 571 W m^{-2} for AM 1.5. The compounded uncertainty from the calibration process is estimated to be 15%.

As shown in Fig. S2 the irradiance used in the high throughput experiments exceeds that of AM 1.5, particularly in the ultraviolet region where $BiVO_4$ is highly absorbing. To calculate the illumination enhancement compared to AM 1.5, the fractional absorption spectrum ($\boldsymbol{A}_{BVO}$) of the as-prepared $BiVO_4$ film was measured using a dual integrating sphere apparatus to simultaneously collect the total reflection and transmission spectra. The calculated absorption spectrum is shown in Figure S2 and is used as a weighting function for the photon flux spectra of the lamp and of AM 1.5. In the 390-600 nm wavelength range, the total $BiVO_4$–absorbed photon flux is 5.6×10^{20} photons m^{-2} s^{-1} for the lamp used in high throughput experiments. Given the calibration uncertainty, this photon flux is a factor of 4.0±0.6 larger than that of the AM 1.5 spectrum.

Using the optical detection system integrated into the photoelectrochemical measurement system, the fractional transmission is calculated from spectra acquired with a reference sample (S_{ref}) and with the illumination turned off (S_{dark}). For a given measured transmission spectrum (S), the fractional transmission is then calculated as $(S - S_{dark})/(S_{ref} - S_{dark})$. For a representative metal oxide catalyst deposited on the FTO/glass substrate, the raw transmission spectra and the calculated fractional transmission are shown in Figure S3. The fractional transmission spectra are measured *in situ* during electrochemical measurements for both catalyst-on-FTO and catalyst-on-$BiVO_4$ libraries, and fractional transmission spectra appear in Eqs. [1]-[3].

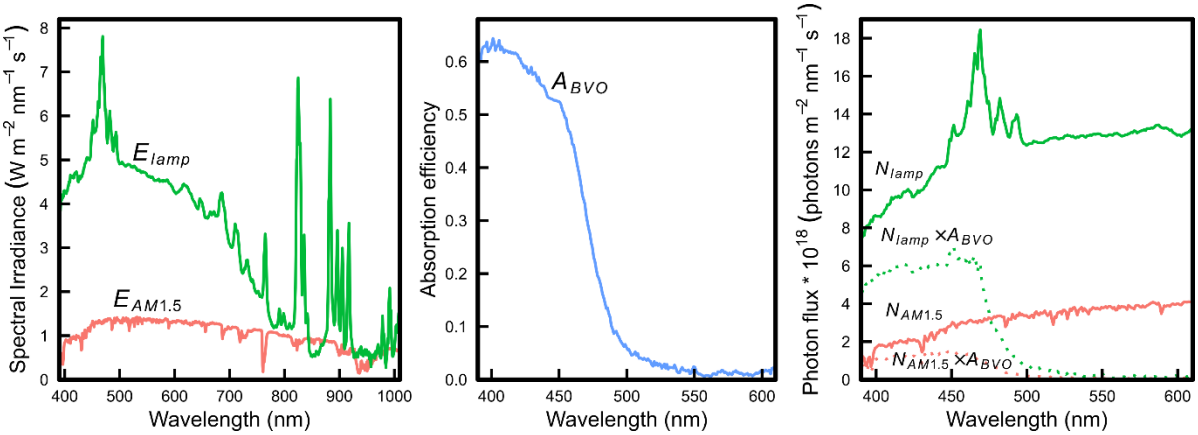

Figure S2. (left) Spectral irradiance of the xenon lamp (green) and ASTM 6173-03 standard for global air mass 1.5 (red). (middle) Fractional absorption spectrum of the BVO light absorber characterized using a dual-integrating sphere system that measures the total spectral transmission and reflection. (right) Photon flux of the incident lamp and AM1.5 (solid lines) and photon flux absorbed by BVO (dotted lines).

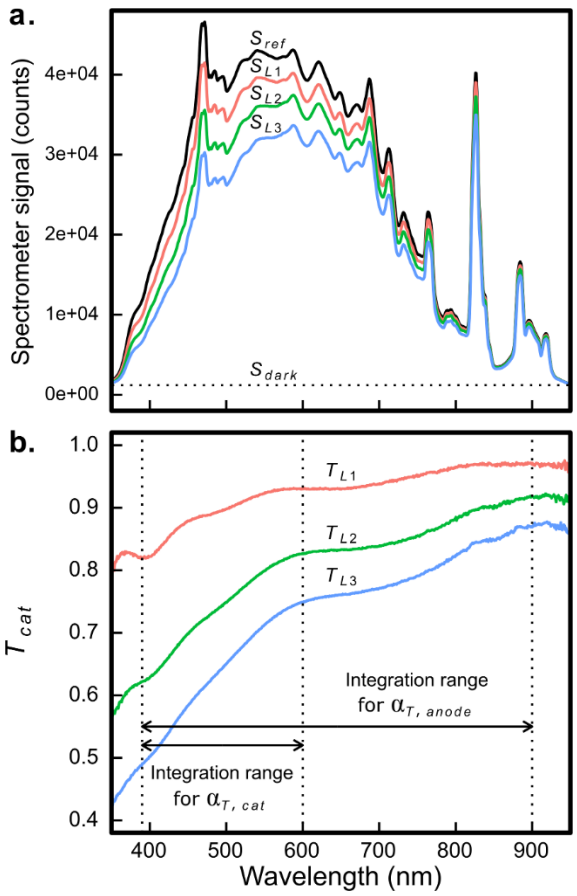

Figure S3. (a) Example spectra are shown for a spectral reference site (S_{ref}, black), a catalyst sample with different loadings (S_{L1}, red; S_{L2}, green; S_{L3}, blue) and a dark scan (S_{dark}, dotted black line) collected with the light source blocked. (b) The fractional spectral transmission T_{cat} is shown for the same catalyst sample with 3 loadings. Wavelength ranges used in calculating optical transmission efficiency $\alpha_{T,cat}$ and $\alpha_{T,anode}$ are labelled.

Electrochemical data processing

Each high throughput cyclic voltammetry (CV) measurement was 64.8 s and swept from 1.23 V to 0.58 V and back to 1.23 V vs. RHE with a sweep rate of 20 mV s^{-1}. Illumination was toggled at approximately 0.5 Hz with illumination on for 1.34 s and off for 0.67 s. The voltage and current were acquired every 0.001 V (0.05 s), yielding 27 data points for each illuminated interval and 13 data points for each dark interval. A transmission spectrum was collected during each illumination cycle and synchronized to the illumination toggling so that the integration time of the spectrum was between approximately 0.63 and 1.3 s of the illumination interval to avoid collection of transient optical signals.

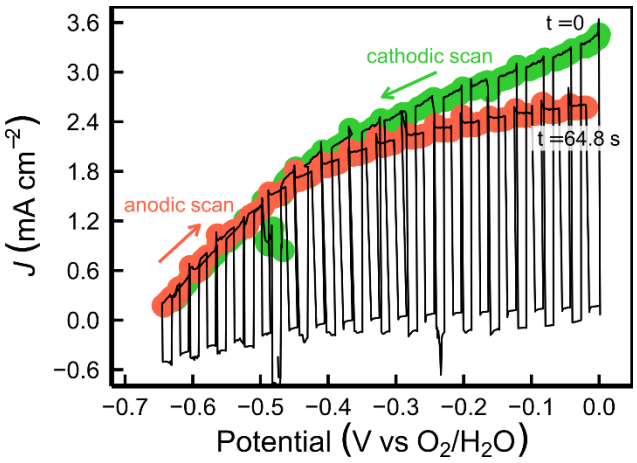

Figure S4. Illumination-toggled cyclic voltammetry (CV) measurement, including the full cathodic and anodic sweeps, highlighted in green and red, respectively.

During initial experiments of duplicate catalyst-coated $BiVO_4$ libraries, we observed that many library samples exhibited substantial degradation in photocurrent during the initial cathodic sweep but that the initial anodic sweep was representative of the photocurrent obtained on subsequent CV cycles. This behavior is similar to that of bare $BiVO_4$ electrodes and in the integrated photoanodes, this transient degradation may be due to the partial exposure of $BiVO_4$ to electrolyte afforded by the non-conformal metal oxide coatings. An example CV showing the lower photocurrent in the anodic sweep compared to the cathodic sweep is shown in Figure S4. To capture the quasi-steady state properties of the photoanodes, the anodic sweep was used for quantifying the photoanode performance.

The photoanode performance metrics are calculated from the anodic sweep of the CV using a polynomial fitting algorithm. The *J-E* data are partitioned according to illuminated and dark intervals, highlighted in red and blue in Figure S5, respectively. To mitigate the influence of the rapid transient current observed with illumination on/off switching, the first 19 data points and last 3 data points from each illuminated interval, and first 9 data points and last data point from each dark interval are omitted from the fit. The remaining points are averaged and the illuminated and dark current signals are each modelled as a third-order polynomial via least-squares fitting. The dark-fitted polynomial is subtracted from the light-fitted polynomial, yielding an anodic photocurrent density signal, $J_{photo}(V)$, (red line) as a function of potential for each photoanode sample.

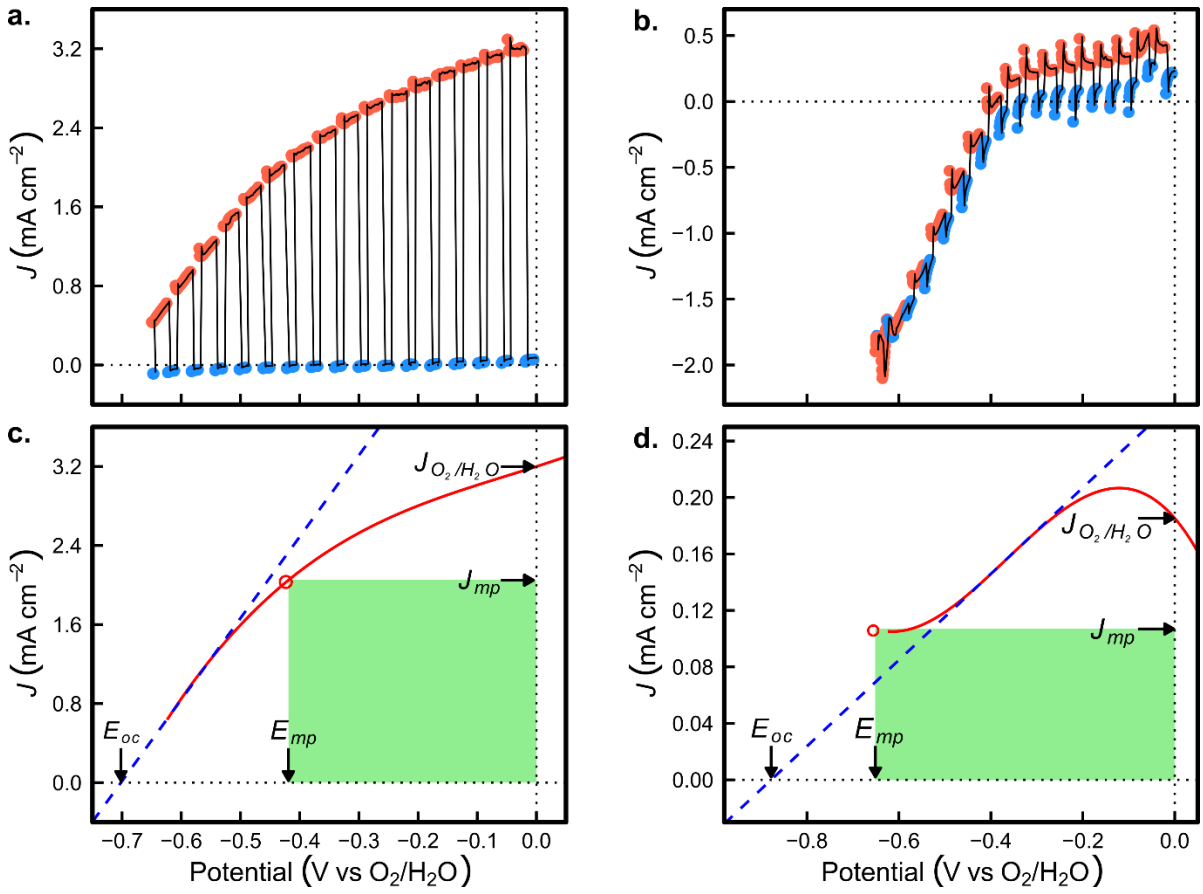

Figure S5. (a) Anodic sweep of a good quality CV and (b) a poor CV with illumination on intervals highlighted in red and illumination off intervals highlighted in blue. (c) Polynomial fit (red line), extrapolated E_{OC} (dashed blue line), maximum power point (red circle), and P_{max} (green area) are shown for a well-behaved CV and (d) poorly-behaved CV. Note that the measured current densities in the poorly-behaved CV are more than 10-fold lower than that of the well-behaved CV, indicating that the analysis technique is suitable for screening the high performing photoanodes but can fail for library samples that exhibit little to no photocurrent.

Figure S5 shows an example of an anodic portion of a CV and the resulting photocurrent density signal, J_{photo}, which is further analyzed to extract P_{max} (green area), J_{O_2/H_2O}, J_{mp}, E_{mp}, and E_{OC}. The data set on the left represents a CV where the algorithm was able to fit a third order polynomial (red line) to the photocurrent and extrapolate the voltage where the photocurrent would be zero (dashed blue line). The data set on the right shows a CV where the fitting algorithm failed, due to substantial dark cathodic current. Fitted photocurrent density signals that exhibit such issues are not analyzed for E_{OC} (missing data points in Figure S6). Since many samples, and especially the best photoanodes, exhibit substantial anodic photocurrent, even at the cathodic terminal of the CV, E_{OC} is estimated using the extrapolation of the terminal slope of the photocurrent polynomial. Since the E_{OC} calculation introduces opportunities for systematic errors and sensitivity to experimental noise, the reported values are considered approximate. The primary performance metrics discussed in the manuscript, J_{O_2/H_2O} and P_{max}, are more robustly determined by the high throughput measurement and data processing.

Photoanode figures of merit for all catalyst loadings L1, L2, L3

The E_{OC} estimates are shown in Figure S6 for all 3 catalyst loadings. In the manuscript, P_{max} is shown for all 3 loadings in Figure 5, and the full library map of J_{O_2/H_2O} is shown In Figure S7.

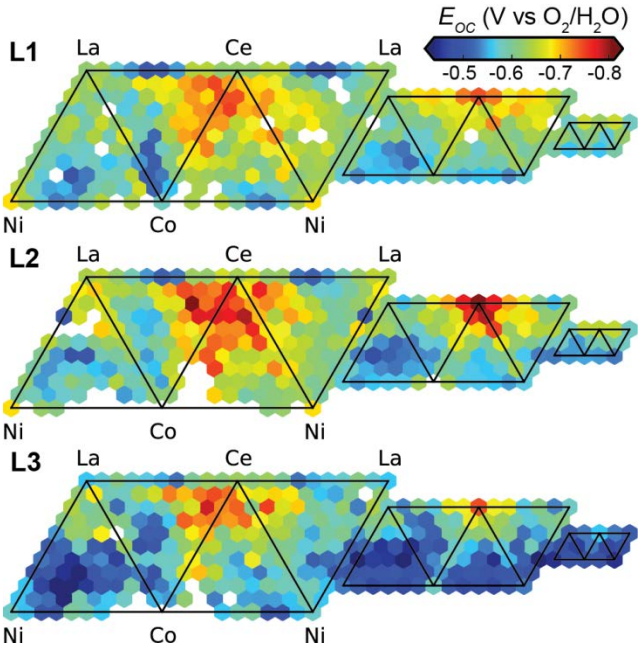

Figure S6. The extrapolated open circuit photovoltage, as calculated from the polynomial fit to the high throughput chopped-illumination CVs and quantified with respect the OER equilibrium potential, is shown for all 3 catalyst loadings of the photoanode library.

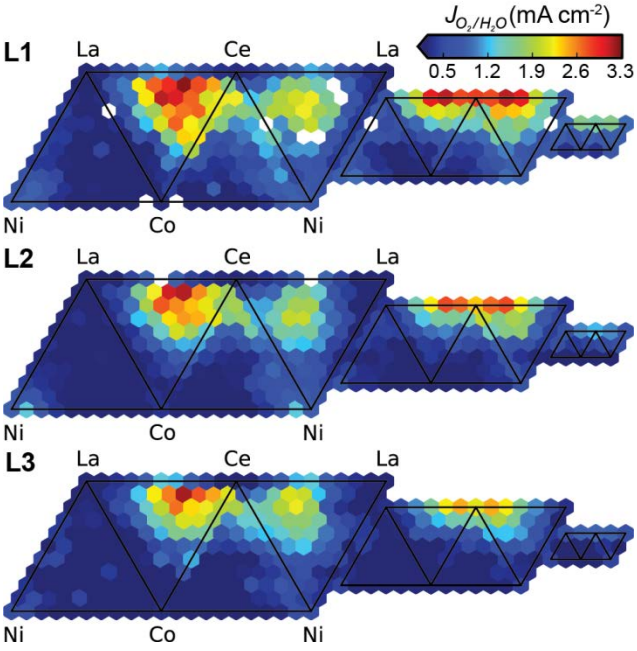

Figure S7. J_{O_2/H_2O} for all three loadings of the (Ni-La-Co-Ce)O_x photoanode library.

Electrocatalyst figures of merit for all catalyst loadings L1, L2, L3

As described in the manuscript, the metal oxide library was synthesized on an FTO-coated glass plate to characterize OER electrocatalytic performance and optical transparency under operating conditions. The maps for loading L3 are shown in the manuscript (Fig. 8) and the full library maps for the catalytic current density and transmission efficiency of $BiVO_4$-absorbable photons are shown in Figures S8 and S9, respectively.

In Figure S10, the combined catalyst efficiency is mapped over its 2 constituent catalyst performance metrics from Figures S8 and S9. The combined catalyst efficiency is mapped over thickness and composition space in Figure S11. The metric for quantifying photoanode performance enhancement with respect to the combined catalyst efficiency is mapped in Figure S12. It is worth noting that for Figures S8, S9, S11 and S12, the data for loading L3 is identical to that of the manuscript figures.

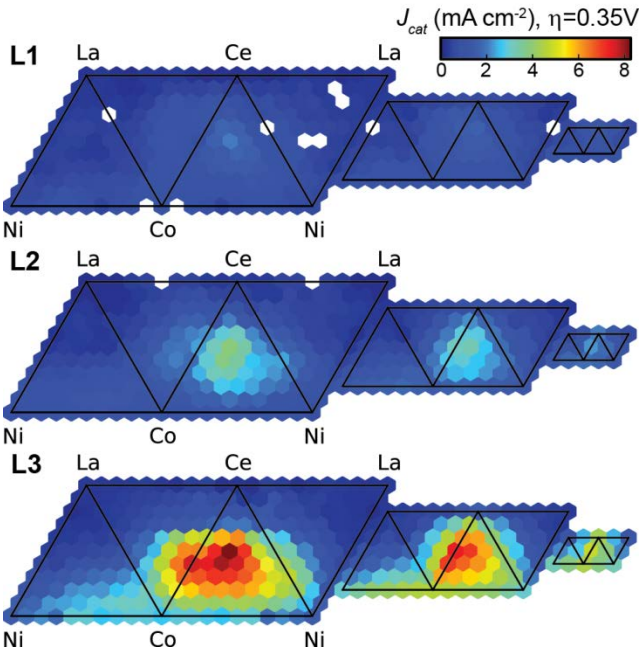

Figure S8. Catalytic current density J_{cat} at 1.58 V vs RHE (η_{OER} = 0.35 V overpotential) for all three loadings in the electrocatalyst library.

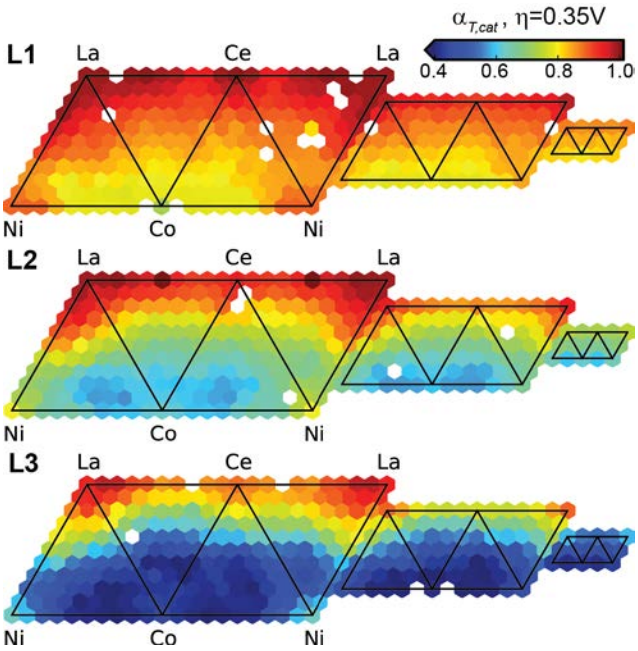

Figure S9. Optical transmission efficiency $\alpha_{T,cat}$ of the catalyst library at 1.58 V vs RHE (η_{OER} = 0.35 V overpotential) for all three loadings.

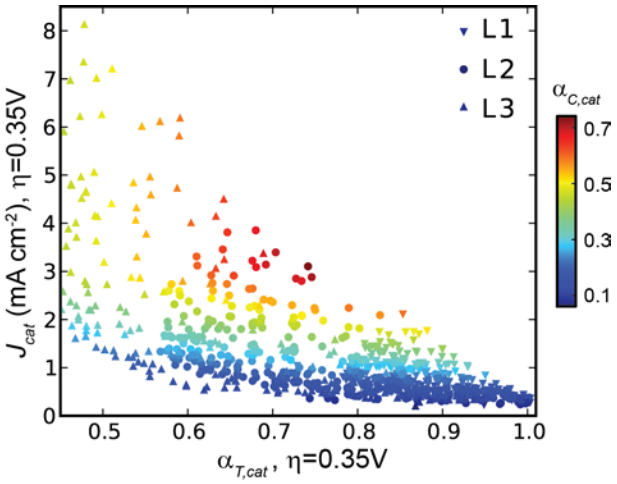

Figure S10. Scatter plot of the unitless combined catalyst efficiency $\alpha_{\mathrm{C,cat}}$ of all three catalyst loadings. Vertical axis is current density J_{cat} at η_{OER} = 0.35 V from Figure S8 and horizontal axis is optical transmission efficiency $\alpha_{T,cat}$ from Figure S10.

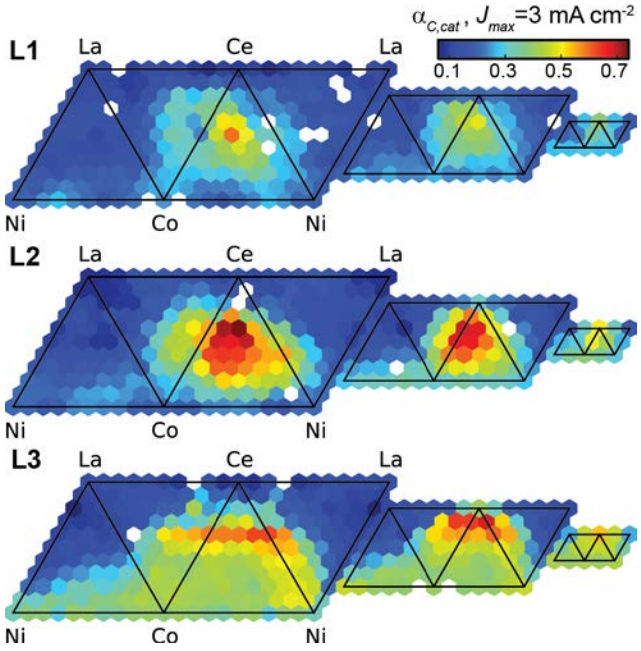

Figure S11. Combined catalyst efficiency $\alpha_{C,cat}$ of the catalyst library at all three loadings for J_{max} = 3 mA cm^{-2}.

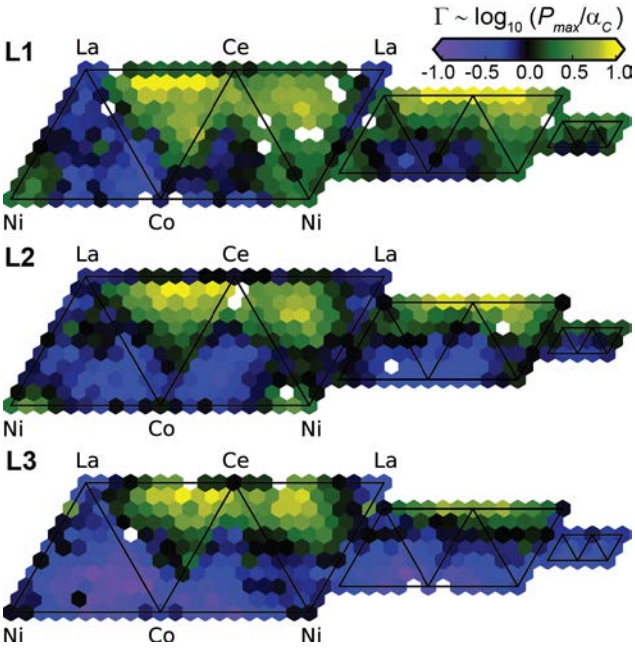

Figure S12. Γ for all three loadings where $\Gamma = \Gamma' - \mathrm{median}(\Gamma')$ and $\Gamma' = \log_{10}\left(\alpha_{C,cat}/P_{\max}\right)$, as discussed in the manuscript.

Optical and power efficiency characterization of the photoanode libraries

The optical transmission of each photoanode sample was measured *in situ* during the high throughput CVs. As noted in the manuscript, this measurement was successful for approximately 97% of the samples, enabling calculation of several optical properties, most notably the consumed optical power ($P_{consumed}$). There is no universal target value for this quantity because highly absorbing photoanodes are desirable, but highly transmissive photoanodes are also desirable for coupling with a tandem photocathode. For high throughput performance mapping, the power conversion efficiency, which is described in the manuscript and discussed further below, is the most useful performance metric. Here we show the composition and loading map of the non-transmitted optical power over the 390-900 nm range. Each $P_{consumed}$ value is calculated using the transmission pattern ($T_{anode}(\lambda)$) from the voltage closest to E_{mp}. As with all optical transmission figures of merit, Co-rich compositions are not very transmissive (high $P_{consumed}$) and transmission for all compositions decreases ($P_{consumed}$ increases) with increasing catalyst loading.

The unique performance of the $Ni_{0.1}La_{0.1}Co_{0.1}Ce_{0.7}O_x$–L1 photoanode sample is discussed in the manuscript due to its high transparency, which exceeds that of bare $BiVO_4$. Figure S14 shows the *in situ* $T_{anode}(\lambda)$ spectrum for this photoanode sample and for the 3 bare $BiVO_4$ samples discussed in the manuscript. While the transmission at wavelengths below that of the $BiVO_4$ band gap is similar, the transmission of $Ni_{0.1}La_{0.1}Co_{0.1}Ce_{0.7}O_x$–L1 is much higher in the rest of the spectral range, especially in the 500-800 nm range that may be well-utilized by an underlying photocathode.

While the power conversion efficiency, $\alpha_{P,anode}$, is only reported at the maximum power point in Figure 10, the high throughput CV data with *in situ* spectroscopy provides the ability to map $\alpha_{P,anode}$ as a function of potential. This potential-dependent efficiency is shown in Figure S15 for the $Ni_{0.1}La_{0.1}Co_{0.1}Ce_{0.7}O_x$–L1 photoanode sample and a representative bare $BiVO_4$ sample. The $Ni_{0.1}La_{0.1}Co_{0.1}Ce_{0.7}O_x$–L1 sample does not show a strong electrochromic effect, so this $\alpha_{P,anode}$ curve is roughly proportional to the $J_{photo}(V)$ signal shown in Figure 3c. The $Ni_{0.1}La_{0.1}Co_{0.1}Ce_{0.7}O_x$–L1 photoanode provides a 20-fold increase in maximum efficiency compared to bare $BiVO_4$, and at the cathodic potentials of interest for coupling with a photocathode, the enhancement is far greater.

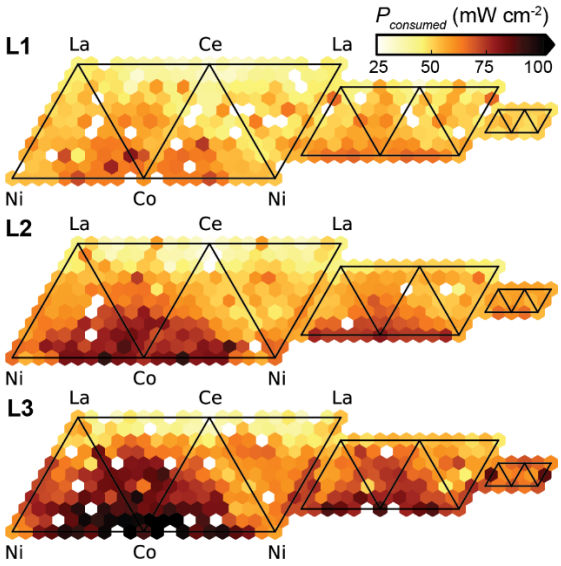

Figure S13. The optical power consumed ($P_{consumed}$) for the operational photoanodes is shown for all 3 loadings.

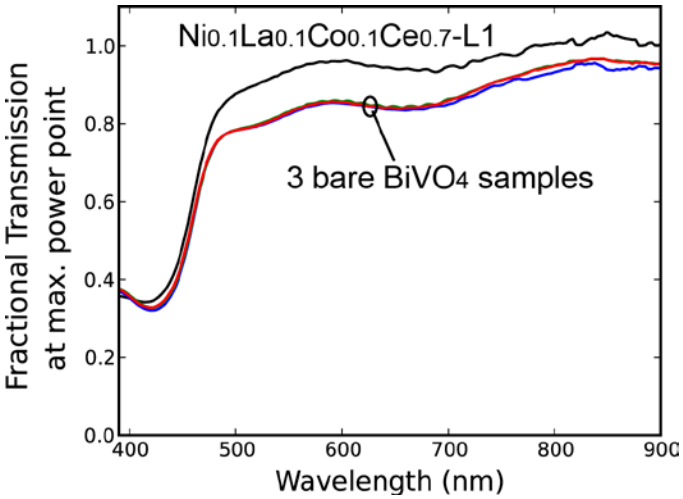

Figure S14. The fractional transmission, $T_{anode}(\lambda)$, near the maximum power point for $Ni_{0.1}La_{0.1}Co_{0.1}Ce_{0.7}O_x$–L1 (black) and 3 bare $BiVO_4$ samples (overlapping red, green, blue curves).

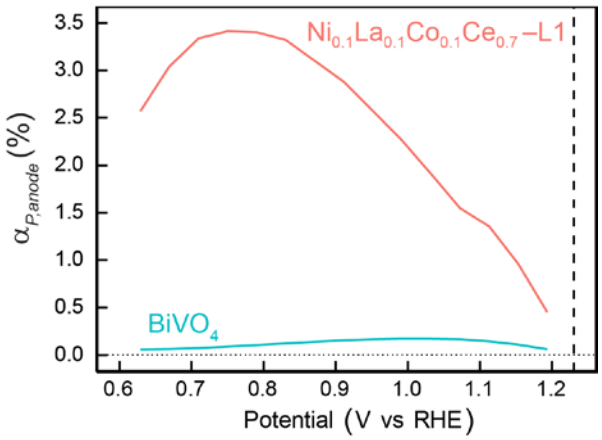

Figure S15. The power conversion efficiency, $\alpha_{P,anode}$, is shown as a function of potential for the $Ni_{0.1}La_{0.1}Co_{0.1}Ce_{0.7}O_x$–L1 and representative $BiVO_4$ photoanodes. For each photoanode, the maximum efficiency (approximately 3.4% and 0.17%, respectively) is observed near the maximum power point. The horizontal dotted line corresponds to 0% efficiency and the vertical dashed line corresponds to the Nernstian O_2/H_2O potential, where $\alpha_{P,anode}$ is 0 by definition.

Characterization of scaled-up photoanode

SEM and EDS analysis of ~1 cm^2 electrodes are shown in Figure S16 and Table S3. The overview image of the uncoated $BiVO_4$ in (a) shows uniform film morphology over 100 µm length scales, while the high-magnification image (b) shows fine grained crystallites that are 50-100 nm in size, comparable to the film thickness. Figures (c) and (d) provide an overview and higher magnification view, respectively, of the as-synthesized inkjet printed catalyst on the $BiVO_4$ film after calcination at 350 °C but prior to any electrochemical testing. The overview image shows significant contrast variation on the 10-100 µm length scale. The features are labelled and were confirmed by EDS analysis of the different regions (data not shown). These labels are also commensurate with the observation of a similar morphology of the bare-$BiVO_4$ in figures (b) and (d). The $La_{0.2}Co_{0.2}Ce_{0.6}O_x$ coating in (b) appears as both light and dark grey areas, which we believe to be thinner and thicker catalyst films, respectively. The higher magnification image of the catalyst reveals morphology on multiple length scales, including sub-50 nm. Within measurement error, the composition of the catalyst layer matches the intended composition of $La_{0.2}Co_{0.2}Ce_{0.6}O_x$ and the composition of the $BiVO_4$ was unaffected by the catalyst deposition and calcination.

After electrochemical testing, the overview image in (e) shows several 10-100 µm regions over which the $BiVO_4$ film has flaked off, exposing the underlying FTO layer. This image also reveals that the light and dark grey areas of thinner and thicker catalyst film appear unchanged. Moreover, EDS indicates that the catalyst composition is unchanged by the extensive PEC testing. Commensurate with the known instability of $BiVO_4$ in pH 13, the PEC experiments increased the overall Bi:V ratio from 1:1 to 2:1. Based upon the change in the absolute Bi and V peak intensity compared to the substrate Si and Sn peaks, it appears that this composition change is due to V loss with no measurable loss of Bi. Similarly, there was no measureable loss of Co, La, or Ce in the PEC experiments. The significant loss of V clearly demonstrates that the discontinuous catalyst film does not physically protect the $BiVO_4$ layer from chemical attack, motivating the exploration of more conformal catalyst coatings.

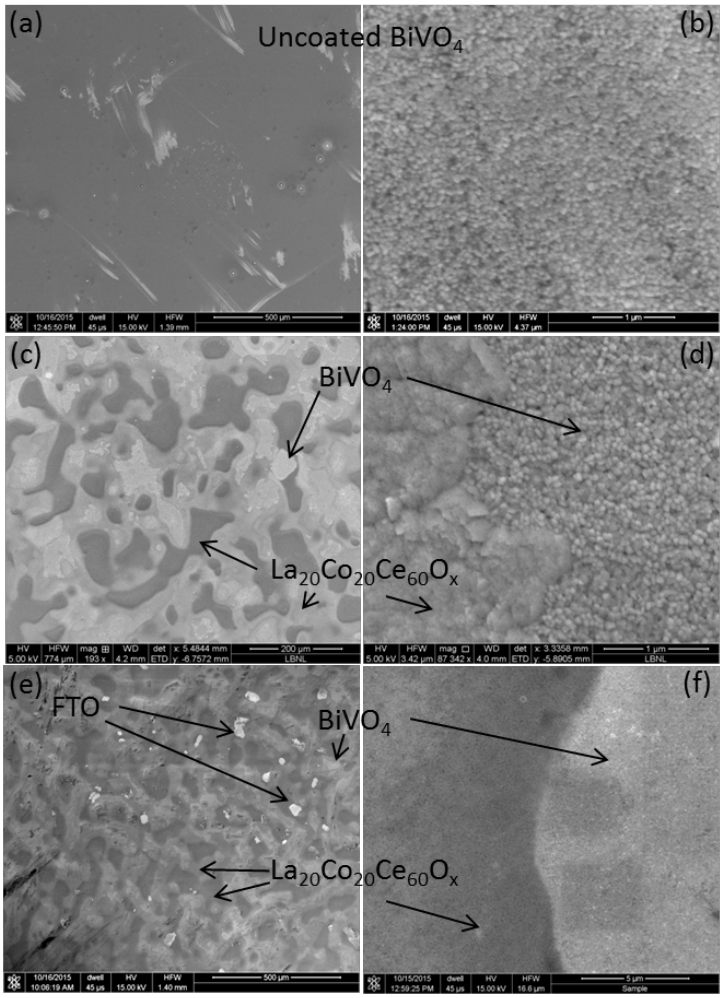

Figure S16. SEM images of the scaled-up (~1 cm^2) electrode: (a) and (b) uncoated $BiVO_4$ film, (c) and (d) $BiVO_4$ film coated with inkjet printed catalyst of target composition $La_{0.2}Co_{0.2}Ce_{0.6}O_x$ as synthesized (before electrochemistry), and (e) and (f) $La_{0.2}Co_{0.2}Ce_{0.6}O_x$ -coated $BiVO_4$ after electrochemical testing. Note the variation in magnification: scale bars represent (a) 500 µm, (b) 1 µm, (c) 200 µm, (d) 1 µm, (e) 500 µm, and (f) 5 µm. The discontinuous catalyst coating of the as-prepared photoanode is apparent in (c). On the nanoscale, the inkjet printed catalyst has a finer particulate structure, which is most apparent in (d). Typical regions of uncoated $BiVO_4$ and thin and thick $La_{0.2}Co_{0.2}Ce_{0.6}O_x$ coating are indicated with arrows, as are some bare FTO regions from the post-PEC image (e).

Table S3. EDS quantification collected while rastering the 15 keV electron beam over large (>1 mm^2) sample areas. For the as-prepared electrode, the Bi:V and La:Co:Ce compositions are each commensurate with the intended compositions of $BiVO_4$ and $La_{0.2}Co_{0.2}Ce_{0.6}O_x$.

	$BiVO_4$ composition		**(La-Co-Ce)O_x Catalyst Composition**		
	at% Bi	**at% V**	**at% La**	**at% Co**	**at% Ce**
uncoated $BiVO_4$	49	51	-	-	-
as-prepared	50	50	22	17	61
post-PEC	63	37	22	17	61